Effects of stratification and shelf slope on nutrient supply in coastal upwelling regions

M. G. Jacox[1] and C. A. Edwards[1]

[1]   An idealized, two-dimensional numerical modeling study is presented to investigate the effects of variable shelf slope and stratification on surface mixed layer (SML) nutrient supply during upwelling. As reported previously, the physical flow regime is governed by a topographic Burger number. Gradual shelf slope and weak stratification concentrate onshore transport in the bottom boundary layer (BBL) while steep slope and strong stratification increase the relative interior transport between the SML and BBL. In 20 day model simulations initialized with a linear nitrate profile, BBL nitrate flux decreases with increasing Burger number. The opposite is true for interior nitrate flux. Upwelling source depth is also investigated and increases more rapidly with weak stratification and steep slope. Both nitrate flux and source depth are well represented by an empirical model approaching an asymptotic value with time. Model experiments representing specific locations in major upwelling systems are analyzed to determine the impact of global variability in physical parameters on event-scale nitrate supply. After 5 days, nitrate flux into the SML is ~45 mmol s^{-1} m^{-1} of coastline at a Peru site, ~30 mmol s^{-1} m^{-1} at northern California and northwest Africa sites, and <2 mmol s^{-1} m^{-1} off Newport, Oregon. BBL flow dominates onshore transport in northwest Africa and northern California runs, while the interior contributes significantly at our Peru and Oregon sites. Nitrate flux estimates based on constant upwelling source depth are strongly dependent on source depth choice at our selected California Current sites and less so at selected Peru and Canary Current sites.

Citation: Jacox, M. G., and C. A. Edwards (2011), Effects of stratification and shelf slope on nutrient supply in coastal upwelling regions, *J. Geophys. Res.*, *116*, C03019, doi:10.1029/2010JC006547.

1. Introduction

[2]   Wind-driven coastal upwelling in eastern boundary current systems (EBCs) transports cold, nutrient-rich water to the surface, placing these regions among the ocean's most productive in terms of both primary production and fish catch [*Chavez and Toggweiler*, 1995; *Pauly and Christensen*, 1995]. The biological importance of EBCs has long been known and they have been subject to intensive study, but questions remain about controls on productivity, which varies widely within and among upwelling systems [*Carr and Kearns*, 2003]. Although new production in EBCs is supported primarily by upwelling of deep nutrients to the euphotic zone [*Dugdale and Goering*, 1967], the relationship between nitrate supply and primary production is unclear [*Chavez and Messié*, 2009].

[3]   The vertical structure of cross-shelf flow has obvious implications for nutrient supply to the euphotic zone, and mooring data show substantial variation in this structure among global upwelling regions [*Smith*, 1981]. Motivated by these observations, *Lentz and Chapman* [2004] (hereafter referred to as LC) developed a simple, steady state theory for two-dimensional wind-driven coastal upwelling as a function of the topographic Burger number

$$S = \alpha N/f, \qquad (1)$$

where α is topographic slope of the continental shelf, N is buoyancy frequency, and f is Coriolis frequency. The theory describes the relative proportion of volume transport in the bottom boundary layer (BBL) and ocean interior. Lower Burger numbers yield cross-shelf flow more concentrated in the BBL. As Burger number increases, surface wind stress is increasingly balanced by the cross-shelf momentum flux divergence rather than bottom stress, and cross-shelf transport occurs increasingly in the interior. Though highly simplified, the steady state theory shows strong quantitative agreement with 2-D model experiments over a linearly sloping shelf and agrees qualitatively with mooring data from the California, Humboldt, and Canary upwelling systems.

[4]   Burger number parameters (topography, stratification, and latitude) vary significantly worldwide (Table 1), motivating our study to investigate their respective roles in determining nutrient supply, and thus new production. While

[1]Department of Ocean Sciences, University of California, Santa Cruz, California, USA.

Table 1. Model Input Parameters for Global Upwelling Regions[a]

Site	Upwelling Season	α (10^{-3})	N (10^{-3} s^{-1})	f (10^{-4} s^{-1})	τ (N m^{-2})	S
Peru	Jul–Sep	8.75	5.85	−0.38	0.11	1.35
Oregon	Jun–Aug	6.7	14.6	1.03	0.03	0.95
N California	May–Jul	5	7.75	0.91	0.18	0.43
NW Africa	Jun–Aug	1.5	6.7	0.54	0.13	0.19

[a]Here α is shelf slope, N is buoyancy frequency, f is Coriolis frequency, τ is surface wind stress, and S is Burger number. The α, N, and f are from *Lentz and Chapman* [2004], and τ is a mean of QuikSCAT alongshore wind stress averaged over the upwelling season.

two-dimensional models have been employed previously to elucidate physical characteristics of upwelling circulation [e.g., *Allen et al.*, 1995; *Lentz and Chapman*, 2004; *Chapman and Lentz*, 2005; *Estrade et al.*, 2008], we are unaware of any that examine the resultant effects on nutrient distribution. *Laanemets et al.* [2009] use the LC theory to explain greater nutrient input along the south coast of the Gulf of Finland than the north coast under equal upwelling favorable winds. While their study demonstrates the potential of the idealized model to explain real world observations, it considers only a single case with weak slope ($\alpha = 0.002 - 0.004$), strong stratification ($N = 0.025$ s^{-1}), and high latitude ($f = 1.25 \times 10^{-4}$ s^{-1}). Building on the results of LC, we examine how nutrient supply and upwelling source depth are affected by physical properties spanning those found in major global upwelling regions.

[5] Although physical transports are determined by the Burger number, nitrate flux is modulated by stratification, bottom slope, and Coriolis frequency independently. Changes to the Burger number through stratification alter the relative fraction of interior and bottom transport, and thus the nutrient supply. However, bottom slope effects are more complex. Weak slope (low Burger number) concentrates flow in the BBL, while a steep slope results in deep water being laterally closer to the coast. Though a greater fraction of transport will be near the bottom for $\alpha = 0.004$ than $\alpha = 0.008$, water of a given depth (and nitrate concentration) must travel only half as far to reach the coast in the latter case. Similarly, increasing Coriolis frequency decreases Ekman transport, but also shifts onshore flow to the BBL.

[6] There are several parts to this study. First, an idealized 2-D numerical model configured to approximate a wide range of upwelling regions is diagnosed for nitrate fluxes and upwelling source depth through time. Though nitrate is chosen here to represent nutrient availability, the approach and conclusions are generally applicable to other macronutrients such as phosphate and silicate. Total surface nitrate, its rate of change, and individual contributions of the BBL and interior are related to the physical constraints of the system, including stratification, shelf slope, wind stress, and latitude. Second, a set of analytical expressions, empirically obtained from model output, are presented to quantify the temporal evolution of upwelled nitrate and characteristic source depth of upwelled waters. Finally, the model is applied to specific locations in global EBCs to illustrate possible controls on nutrient availability.

2. Regional Ocean Modeling System Model

[7] Numerical model experiments are performed using the Regional Ocean Modeling System (ROMS [*Shchepetkin and McWilliams*, 2005; *Haidvogel et al.*, 2008]) with a two-dimensional (no alongshore variation) setup similar to that of LC. A periodic channel is constructed with two alongshore grid points, a wall 160 km offshore, and 1 km horizontal grid resolution. There are 100 vertical levels, concentrated near the surface and bottom to ensure adequate resolution of the boundary layers. While fewer vertical levels could be used without altering the model substantively, high vertical resolution allows for cleaner calculation of model diagnostics, specifically advective and diffusive tracer fluxes. Bottom depth increases linearly from a minimum of 20 m at the coast to a maximum of 1000 m offshore. Turbulence closure is handled by the Mellor-Yamada level 2.5 scheme, and there is no explicit lateral mixing. The domain is initiated from rest and forced by a spatially and temporally uniform upwelling-favorable alongshore wind stress. Except where otherwise noted, wind stress $\tau = 0.1$ N m^{-2} and Coriolis frequency $f = 10^{-4}$ s^{-1}.

[8] To determine sensitivity of the model to variations in its parameters, a number of configurations were explored. We examined several vertical mixing schemes ($k - \omega$ and $k - \epsilon$ in generic length scale [*Umlauf and Burchard*, 2003] and K profile parameterization [*Large et al.*, 1994]) in place of Mellor-Yamada level 2.5. Alternative offshore boundary conditions tested include a closed boundary 500 km offshore, a highly viscous sponge added near the boundary, and a radiation boundary condition. Finally, horizontal resolution was increased from the default 1 km to 0.5 km and 0.25 km. While small-scale circulation features are altered by these configuration changes, implications are negligible for the net transport processes of interest here.

[9] LC investigated the effect of Burger number on cross-shelf transport by varying stratification while holding both Coriolis frequency and shelf slope constant. Here, an initial set of 12 model runs intended to replicate their findings produced similar results and matched the theory well after several days of spin-up. Additionally, a set of 25 model runs were performed with shelf slopes of 0.002, 0.004, 0.006, 0.008, and 0.010 and buoyancy frequencies of 0.004, 0.008, 0.012, 0.016, and 0.020 s^{-1}. These parameters were chosen to cover the range of conditions found in the major global upwelling regions and to investigate stratification and slope effects independently. Sensitivity to changes in Coriolis frequency was not examined as thoroughly; however three model configurations with wide-ranging Burger numbers were run with Coriolis frequency varied between 0.4×10^{-4} and 1.3×10^{-4} s^{-1}. To track nutrient fluxes, a passive tracer representing nitrate (and herein referred to simply as nitrate) was introduced with an initial profile increasing linearly from 0 μM at the surface to 30 μM at 200 m depth and remaining constant below 200 m.

[10] Finally, several model runs were performed to more closely represent specific global upwelling regions. These runs are still idealized in that they are 2-D and have linearly
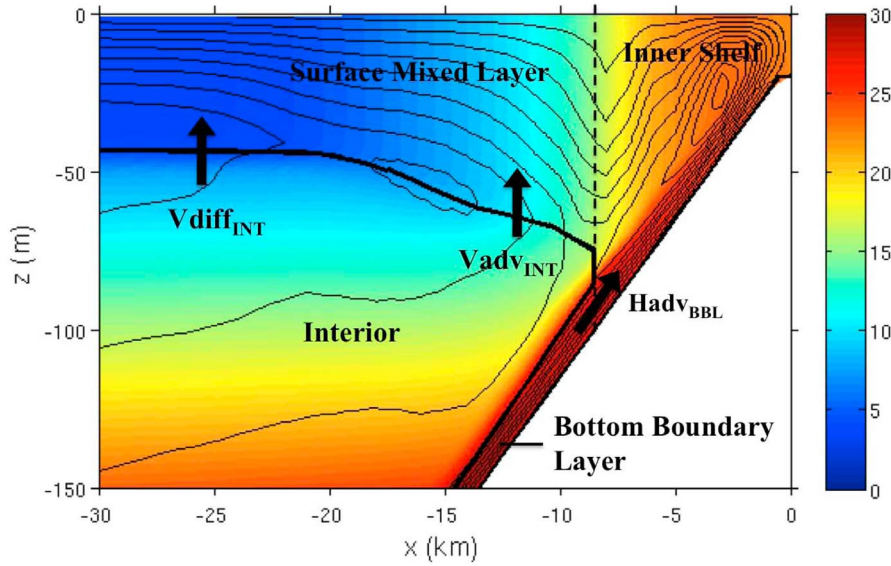
Figure 1. Streamlines (thin black lines) overlaid on nitrate concentration (μM, color) for model output on day 10, with $\alpha = 0.010$ and $N = .004$ s^{-1}. Thick black lines mark the surface and bottom mixed layers and extent of the inner shelf (dashed). Arrows indicate contributions to nitrate flux, which are horizontal advection in the bottom boundary layer (Hadv$_{BBL}$) and vertical advection (Vadv$_{INT}$) and diffusion (Vdiff$_{INT}$) in the interior. Offshore advection in the surface mixed layer (Hadv$_{OFF}$) and mixed layer deepening ($\mathcal{E}$) are not shown. These five terms make up the surface mixed layer budget as outlined in equation (5).

sloping bottom topography, surface wind forcing that is uniform in space and time, and constant stratification. However in each case, the buoyancy frequency, bottom slope, latitude, wind stress magnitude, and initial nitrate profile are characteristic of the region of interest. The locations chosen are those discussed in LC, where mooring data provide an accurate determination of stratification in the water column.

3. Methodology

[11] For budgeting purposes, we divide the model domain into four regions: the inner shelf, the surface and bottom mixed layers, and the interior between them. Near shore, bottom and surface mixed layers converge, and we define here the region where their boundaries are separated by less than 10 m as the inner shelf. Figure 1 illustrates these regions and also shows instantaneous streamlines of the flow superposed on nitrate concentration for a representative model run. In our configuration, x denotes cross-shelf distance with the coastal boundary, $x = 0$, located at the eastern edge. The vertical coordinate is z, directed upward, with the unperturbed ocean surface at $z = 0$. The ocean bottom is given by $z_b(x) < 0$, and the free surface is denoted $\zeta(x, t)$.

[12] Several approaches to define the surface mixed layer (SML) are possible. LC used the first zero crossing of cross-shelf velocity (the depth at which cross-shelf transport switches from offshore to onshore). An alternative is the depth at which temperature or density differs by a fixed amount from the surface value. A third definition, the PRT depth [*Pollard et al.*, 1973], scales mixed layer depth as $u_*/(Nf)^{1/2}$ where u_* is shear velocity. *Lentz* [1992] found the PRT depth to effectively capture subtidal mixed layer depth variability at locations in the California, Peru, and Canary

Current systems. We found that surface layer offshore flow in our model is best diagnosed by high vertical viscosity coefficients and used a value of $10^{-3.5}$ m^2 s^{-1} to define the base of the SML (z_{sml}). This approach aligns this boundary well with streamlines near the upwelling front. The height of the BBL is defined in the same manner.

[13] We consider the total nitrate, $\mathcal{N}_T$, contained within a control volume encompassing the SML and inner shelf region from a predefined offshore distance ($x_o = -100$ km) to the coast

$$\mathcal{N}_T(t) = \int_{x_o}^{0} \int_{z_0(x,t)}^{\zeta(x,t)} N(x, z, t)\, dz\, dx. \tag{2}$$

Here $N(x, z, t)$ indicates nitrate concentration and

$$z_0(x, t) = \begin{cases} z_{sml}(x, t) & x < x_i \\ z_b(x) & x \geq x_i, \end{cases} \tag{3}$$

where x_i is the x coordinate of the inner shelf boundary.

[14] For a general control volume, Ω, and assuming no internal sources or sinks, changes to $\mathcal{N}_T$ in time are given by the combination of advective and diffusive nitrate fluxes, $\mathcal{F}$, across the bounding control surface, Ω_S, and nitrate that is captured (or lost) by expansion (or contraction) of Ω

$$\frac{d\mathcal{N}_T}{dt} = -\int_{\Omega_S} \mathcal{F} \cdot \mathbf{n}\, dS + \int_{\Omega_S} N(\mathbf{u_S} \cdot \mathbf{n})dS. \tag{4}$$

The outward normal is denoted $\mathbf{n}$, and $\mathbf{u_S}$ represents the velocity of the control surface. To understand the meaning of the second term, it is helpful to consider the simple
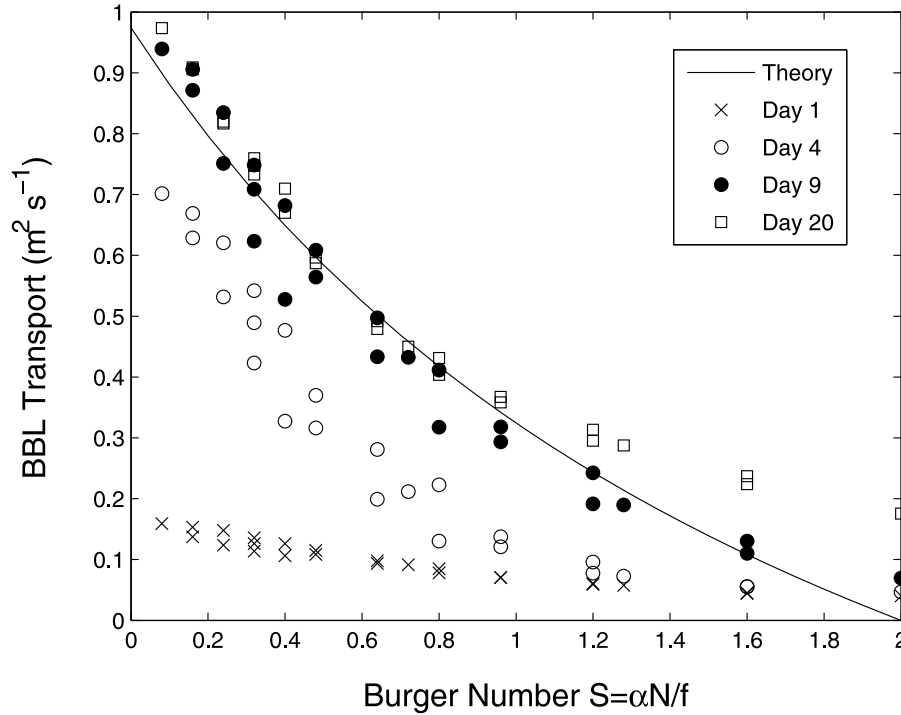
Figure 2. Evolution of bottom boundary layer transport as a function of Burger number. For each model run, transport is calculated at the offshore distance where bottom depth is 90 m, as with *Lentz and Chapman* [2004]. Shown for comparison is their steady state theory. Volume transport is per meter of coastline.

(though unrealistic) case in which $\mathcal{F} = 0$ (e.g., with zero velocity and constant nitrate distribution) but the control volume is expanding (i.e., $\mathbf{u_S} \cdot \mathbf{n} > 0$). In this circumstance, nitrate initially outside the control volume boundary accumulates within the volume as it expands, increasing total integrated nitrate, $\mathcal{N}_T$.

[15] For our configuration, we neglect horizontal diffusion and decompose the first term on the right hand side of equation (4) into three advective fluxes and one diffusive flux, each illustrated in Figure 1. Thus,

$$\frac{d\mathcal{N}_T}{dt} = \int_{z_b}^{z_{sml}} uN\bigg|_{x_i} dz - \int_{x_o}^{x_i} (\mathbf{u} \cdot \mathbf{n})N\bigg|_{z_{sml}} dx$$

$$+ \int_{z_{sml}}^{\zeta} uN\bigg|_{x_o} dz + \int_{x_o}^{x_i} K_v \frac{dN}{dz}\bigg|_{z_{sml}} dx + \mathcal{E}, \qquad (5)$$

where u is the fluid velocity in the x direction and K_v represents the vertical diffusion coefficient for nitrate. The velocity normal to the SML boundary, $z_{sml}(x, t)$, is $\mathbf{u} \cdot \mathbf{n}$. Owing to the aspect ratio, $\mathbf{u} \cdot \mathbf{n}$ appears overwhelmingly vertical when viewed schematically, but horizontal transports across this boundary are numerically sizeable. The terms on the right hand side of equation (5) represent (1) transport across the inner shelf boundary associated with BBL advection (Hadv$_{BBL}$), (2) transport between the ocean interior and SML (Vadv$_{INT}$), (3) horizontal advection within the SML across $x = x_o$ (Hadv$_{OFF}$), (4) vertical diffusion between the interior and SML (Vdiff$_{INT}$), and (5) changes in

$\mathcal{N}_T$ due to shifts in the SML depth and the inner shelf boundary ($\mathcal{E}$). All terms in equation (5) are calculated and compared using discrete approximations appropriate for the model grid. Advective and diffusive fluxes are determined from model state vector output, recorded every 6 h. Changes to total nitrate as well as the contribution due to mixed layer deepening and inner shelf boundary adjustment are calculated using time differences between model output.

4. Results

4.1. Model Results

[16] As discussed by LC, physical transports are dependent on the Burger number, which combines three independent physical parameters. Here we investigate each component separately as they impact tracer advection in different ways, discussed in section 1. A total of 25 model runs are presented that encompass shelf slopes from 0.002 to 0.010 and buoyancy frequencies from 0.004 to 0.020 s^{-1}. The sensitivity to Coriolis frequency is also considered.

[17] Cross-shelf transport develops over several days and agrees well with the LC steady theory after day 9 (Figure 2), though BBL transport is greater in the model than the theory for higher Burger numbers ($\gtrsim 1$) and longer integration times. LC also noted this and found that bottom stress decreases with increasing Burger number, but not as much as predicted by the theory. In all cases, upwelling-favorable wind stress drives a subsurface structure consisting of an offshore region with approximately level isopycnals, a midshelf region characterized by sloping isopycnals, and the inner shelf zone
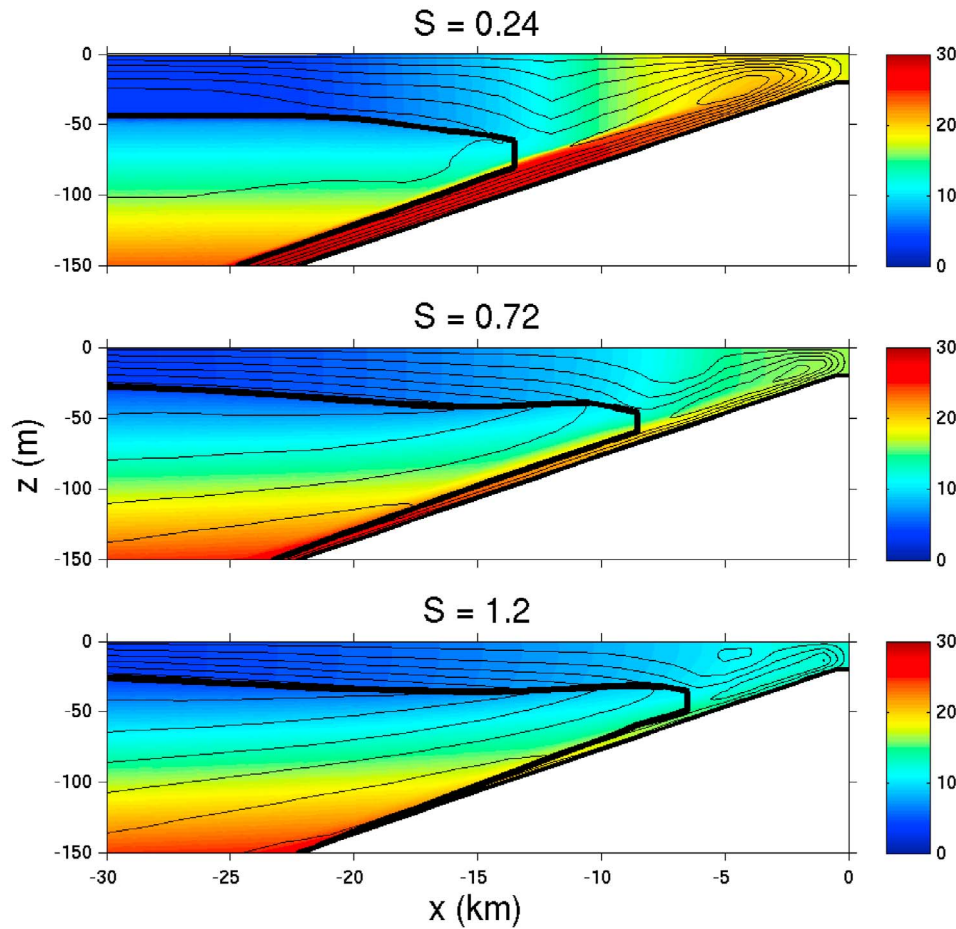
Figure 3. Mixed layers, inner shelf, nitrate, and streamlines are depicted as in Figure 1, for varying Burger numbers on day 10. For all, $\alpha = 0.006$. Buoyancy frequencies are (top) 0.004 s^{-1}, (middle) 0.012 s^{-1}, and (bottom) 0.020 s^{-1}.

where bottom and surface mixed layers merge. Under sustained surface forcing an upwelling front develops, as described by *Allen et al.* [1995]. The upwelling front is marked by strong turbulence and a locally deepened SML (deeper in weakly stratified waters) that typically sets the offshore boundary of the inner shelf. Inshore of the front the model produces onshore flow near the bottom, offshore flow near the surface, and some recirculation at middepths (Figure 3). In certain cases, such as the $S = 1.2$ case in Figure 3, recirculation occurs within the front. With time the front and associated coastal jet strengthen and move offshore at an approximately constant rate as with *Austin and Lentz* [2002]. Figure 4 shows the offshore expansion of the inner shelf with time, and its dependence on slope and stratification. Strong stratification and steep slope ($\alpha N \gtrsim 10^{-4}$ s^{-1}) produce an inner shelf that is confined close to shore, typically within 10 km even after 10–20 days of upwelling. In contrast, weak stratification and gently sloping topography can produce an inner shelf that rapidly extends its offshore reach. Coriolis frequency also impacts the inner shelf extent (not shown); at a given time, the inner shelf extends further offshore at lower latitudes.

4.1.1. Nitrate Fluxes

[18] At low Burger numbers, flow is concentrated in a thick BBL as evidenced by the cross-shelf stream function
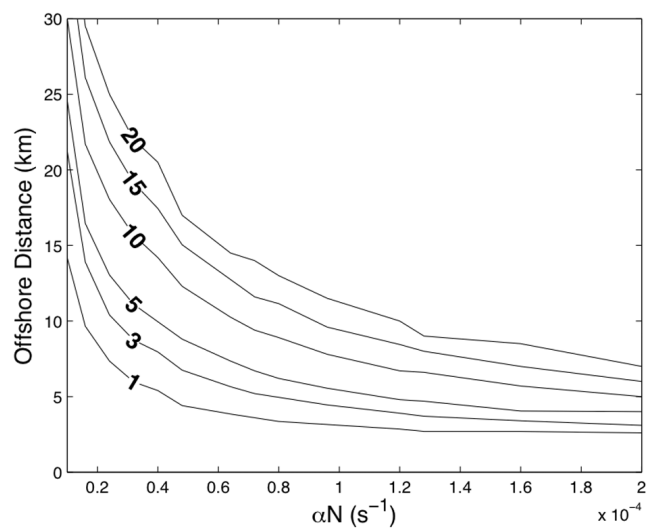

Figure 4. Evolution of the inner shelf and its dependence on Burger number. Distance is measured from the coast to the offshore boundary of the inner shelf. Contours indicate time in days.
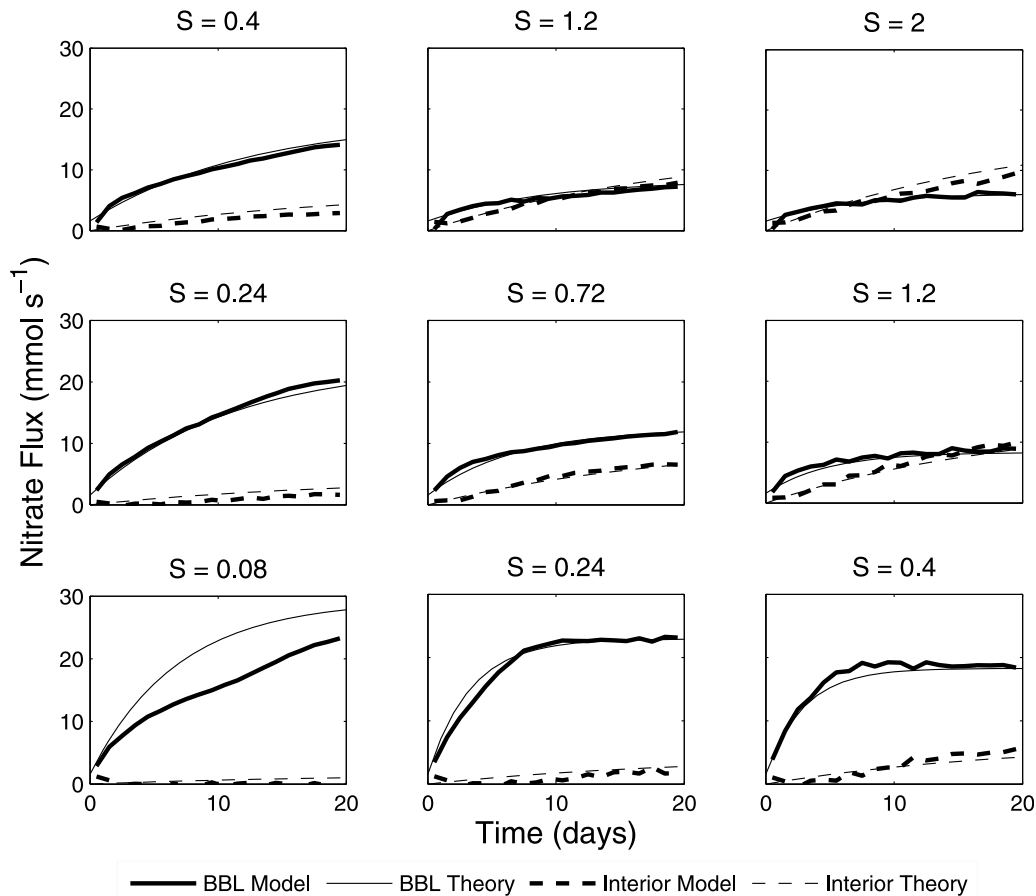
Figure 5. Time evolution of BBL and interior advective nitrate fluxes. Buoyancy frequency increases from bottom to top with values of 0.004, 0.012, and 0.020 s^{-1}. Topographic slope increases from left to right with values of 0.002, 0.006, and 0.010. Coriolis frequency in all cases is 10^{-4} s^{-1}. Thick lines are fluxes calculated from model output, and thin lines are fluxes calculated from the empirical model described by equation (8) and Table 2.

(Figure 3). Deep, high-nitrate (~30 μM) water is rapidly transported onshore in the BBL, mixes in the inner shelf, and moves offshore in the SML. Strong stratification (higher Burger number) produces a thin BBL and shifts streamlines to the interior. For $S = 1.2$, substantial upwelling of intermediate nitrate concentrations (5–15 μM) is visible offshore of the upwelling front, extending ~20 km from the coast. In all three cases shown in Figure 3, surface nitrate at the inner shelf boundary is ~10 μM on day 10. The cross-shelf nitrate gradient is stronger at low Burger numbers, producing a more rapid decrease in nitrate away from the upwelling front. Surface transport offshore of the active upwelling zone is independent of Burger number, though streamlines are concentrated in a shallower SML in strongly stratified systems.

[19] In the model, nitrate is a conserved passive tracer, with no sources or sinks. Nitrate fluxes are calculated through time, and nitrate is assumed to be available for biological uptake upon reaching the SML. Interior and BBL nitrate fluxes and their dependence on stratification and slope over the first 20 days of model runs are shown in Figure 5. At low Burger numbers a large fraction of transport is concentrated in the BBL and deep, nitrate-rich water is carried efficiently

to the surface. Higher Burger numbers produce a greater fraction of onshore transport in the interior of the water column, increasing nitrate advection from the interior to the surface. Since bottom flow draws from deeper source waters than interior flow, upwelling in the BBL is typically the dominant contributor to total nitrate flux, even in cases where interior transport exceeds BBL transport. In our highest Burger number case ($S = 2$), the source of upwelled water is primarily the interior of the water column; however, interior and BBL nitrate fluxes are comparable through much of the run. In this case, weak BBL transport is able to produce significant nitrate flux when combined with high BBL nitrate concentrations.

[20] The results of Figure 5 are of course dependent on our choice of initial nitrate profile. The linearly increasing nitrate profile is a good qualitative representation, but arguably too simplistic for real systems. For comparison, we show the same model runs initialized with a real nitrate profile taken off the Oregon coast at ~45 N and obtained from the Global Ocean Ecosystems Dynamics (GLOBEC) database. This profile has nitrate concentrations that are low in the upper 20 m (≤2.5 μM), increase rapidly below the SML to ~27 μM at 100 m depth, and increase gradually at greater
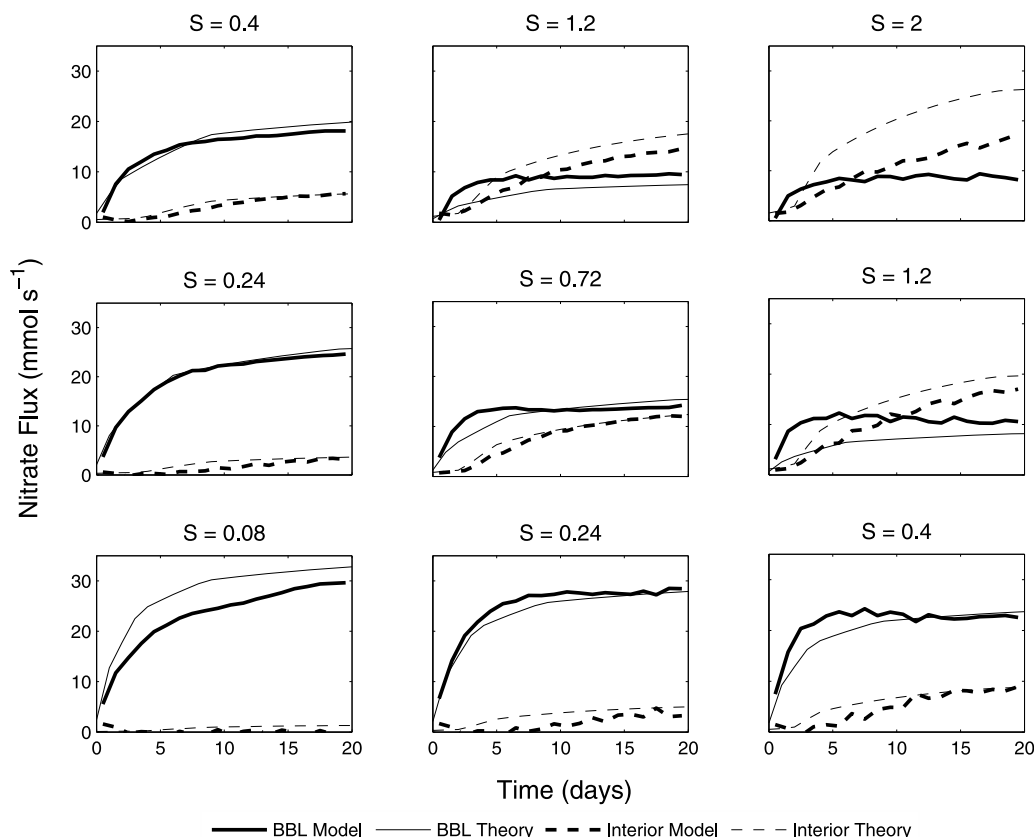
Figure 6. Empirical model of nitrate flux based on upwelling source depth. Slope, stratification, and Burger number are as in Figure 5. The initial nitrate profile is a real profile off the Oregon coast obtained from the GLOBEC database, rather than the idealized profile used for Figure 5. Actual nitrate fluxes as calculated from ROMS output are shown as thick solid and dashed lines for the BBL and interior, respectively. Thin solid and dashed lines are empirical model fluxes calculated from equations (9)–(11) and Table 2. Note that in the highest Burger number case ($S = 2.0$, top right), theoretical BBL transport, and therefore empirically modeled BBL nitrate flux, is zero.

depths, reaching 34 μM at 200 m. There are clear differences between results from the idealized profile (Figure 5) and the real one (Figure 6). For example, nitrate fluxes resulting from the real profile initially increase more rapidly owing to high nitrate concentrations available closer to the surface. However, the qualitative relationship between BBL and interior nitrate fluxes remains unchanged; the BBL dominates at lower Burger numbers and the two components are comparable in magnitude at higher Burger numbers.

[21] Figure 7 presents flux contributions from interior advection, BBL advection, and mixed layer deepening on day 15. The combination of bottom and interior advective fluxes, interior diffusion, and mixed layer deepening gives total nitrate available for new production in the SML. Interior and BBL nitrate fluxes are strongly dependent on Burger number; as Burger number increases, interior flux increases and BBL flux decreases. BBL flux is skewed slightly with weak slope transporting nitrate to the surface more efficiently than weak stratification (for a given Burger number, nitrate flux per unit upwelled volume is greater with weak slope than weak stratification). Similarly for interior flux, steep slope transports nitrate to the surface more efficiently than strong stratification. Vertical diffusion is a rela-

tively small contributor to nitrate supply (1–3 mmol s^{-1}, not shown), but is greatest in weakly stratified water with weak topographic slope. As the SML deepens, it incorporates nitrate previously beneath it. This contribution is greater in weakly stratified conditions, as the mixed layer deepens more rapidly and reaches greater depth in a given time. It is also greater in regions of steep slope; strong interior transport carries high nitrate to the base of the SML where it is entrained as the SML deepens. In sum, total advective nitrate fluxes are greatest with weak stratification and slope ($S \ll 1$), diffusion is small but greater in weakly stratified waters, and nitrate added due to mixed layer deepening is greatest with steep slope and weak stratification. The net effect of these contributions is that total nitrate in the SML after a period of sustained upwelling is primarily dependent on stratification, with the most nitrate available in weakly stratified waters.

4.1.2. Upwelling Source Depth

[22] Understanding the source depth of upwelling allows for more general questions than those of macronutrient supply. To calculate source depth, we introduce a tracer C increasing linearly with depth, and define the "source tracer concentration" ($\mathcal{S}$) as tracer flux divided by volume transport. This quantity is determined at the inner shelf boundary
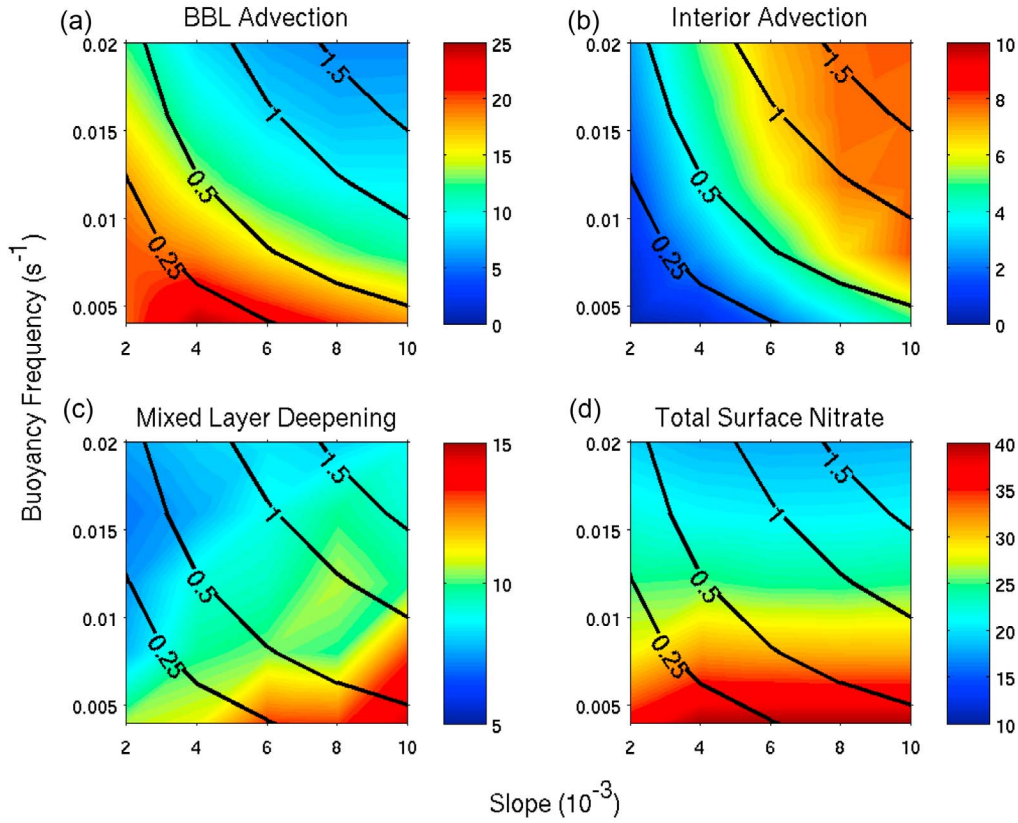
Figure 7. Snapshots of nitrate flux components (in color) on day 15, with Burger number indicated by contours. Nitrate fluxes due to advection in the (a) BBL and (b) interior (mmol s^{-1}), (c) flux due to mixed layer deepening (mmol s^{-1}), and (d) total nitrate in the surface mixed layer within 100 km of the coast on day 15 (10^3 mol N). Note different scales for each. The 25 model runs are represented covering slopes of 0.002–0.010 and buoyancy frequencies of 0.004–0.020 s^{-1}.

for BBL flux and at the base of the SML for interior flux. Specifically,

$$\mathcal{S}_{BBL} = \frac{\int_{z_b}^{z_{sml}} uC \bigg|_{x_i} dz}{\int_{z_b}^{z_{sml}} u \bigg|_{x_i} dz} \qquad (6)$$

$$\mathcal{S}_{INT} = \frac{\int_{x_o}^{x_i} (\mathbf{u} \cdot \mathbf{n})C \bigg|_{z_{sml}} dx}{\int_{x_o}^{x_i} (\mathbf{u} \cdot \mathbf{n}) \bigg|_{z_{sml}} dx}. \qquad (7)$$

Because the initial tracer profile increases monotonically from the surface to the sea floor (unlike our idealized nitrate profile), source tracer concentration can be mapped to source depth. Of course, not all upwelled water originates exactly from this depth, but it is a useful integrated measure of the characteristic depth of upwelling at any given time.

[23] Figure 8 illustrates time evolution of interior and BBL source depth over 20 days of model simulations for a range of Burger numbers. Figure 9 shows snapshots of source depths in all 25 model configurations after 10 and 20 days of model integration. In the BBL, steep slope and

weak stratification produce the greatest source depth. Strong BBL transport carries deep water onshore rapidly in weakly stratified waters. Also, since deep water is closer to shore in steep slope cases, it reaches the surface faster with the same horizontal velocity (compare Figure 1 to Figure 3 (top), which has the same stratification but different slope). In runs with weak stratification and steep slope, source depth exceeds 200 m by day 10 and nitrate advection in the BBL is approximately constant after this time (Figure 5). The asymptotic nitrate flux is set by the steady state BBL transport and maximum nitrate at depth (30 μM). By day 20, only strongly stratified cases have BBL transport originating from less than 200 m depth.

[24] The source depth of upwelled water in the interior depends primarily on topographic slope (Figure 9). Interior transport occurs throughout the region between bottom and surface mixed layers (Figure 3). As with BBL source water, steeper slope configurations have deeper water available at a given distance offshore. This deep water has a shorter path length to reach the upwelling zone than in weak slope cases and reaches the surface sooner with the same horizontal velocity. Stratification appears to become more important at longer times, with weak stratification producing deeper source water after 20 days. By the end of the model run, weak stratification over a steep shelf produces interior upwelling from the greatest depths, approximately 120 m.
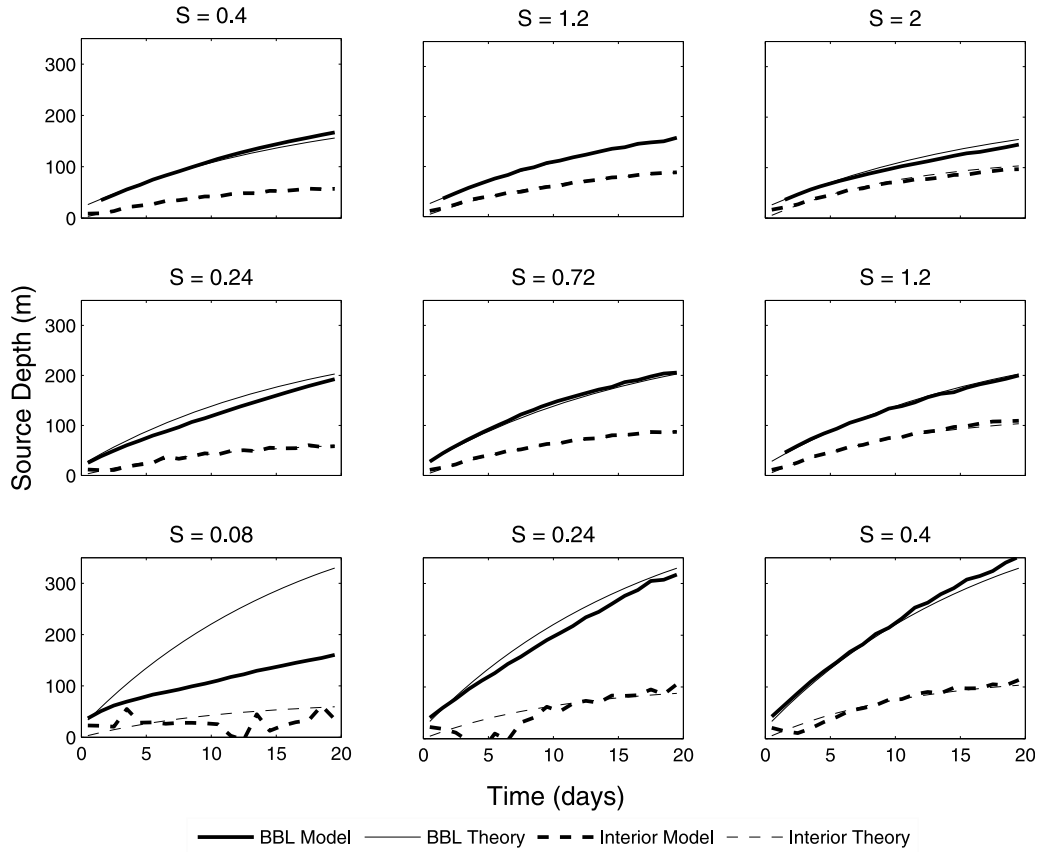
Figure 8. Time evolution of numerical model BBL (thick solid) and interior (thick dashed) upwelling source depths along with those predicted by the empirical model (thin lines). Empirical model approximations come from equation (9) with parameterizations in Table 2. Slope, stratification, and Burger number are as in Figure 5.

4.1.3. Sensitivity to Wind Stress and Latitude

[25] Thus far, Coriolis frequency and wind stress have been held constant at $f = 10^{-4}$ s^{-1} and $\tau = 0.1$ N m^{-2}, respectively. Since both vary significantly across global upwelling regions, their influence on results was investigated. Theoretical Ekman transport is proportional to wind stress, and in model runs where surface forcing is reduced, BBL and interior transport are reduced proportionally. However this transport reduction is not proportional to the nitrate flux reduction. For any model time, the source depth (and therefore nitrate concentration) is greater for a strongly forced case than a weakly forced one. Because reduced wind stress decreases upwelled volume as well as nitrate concentration within upwelled water, the net result is a non-linear relationship between wind stress and advective nitrate flux (Figure 10). Assuming that nitrate flux scales like volume transport would overestimate flux for winds weaker than the reference case (τ_o) and underestimate it for stronger winds. This effect is independent of Burger number; nitrate flux is altered to the same degree in cases of wide ranging slope and stratification.

[26] The impact of changing Coriolis frequency is more complex. In this case, not only is Ekman transport affected, but also Burger number; both are proportional to $1/f$. At lower latitudes, Ekman transport increases, but a greater fraction derives from the interior. To assume that BBL flux should scale with $1/f$ (like transport) overestimates flux at latitudes lower than the reference (f_o) and underestimates it at higher latitudes (Figure 11). The opposite is true for interior flux. It is not our goal to provide an accurate measure of the scaling of nitrate flux with latitude, merely to point out that at low latitude, gains in nitrate flux due to stronger upwelling are partially offset by a shift in upwelling from the BBL to the interior.

4.2. Empirical Model

[27] For a given model latitude, surface forcing, and initial nitrate profile, the magnitude of each nitrate flux component into the SML is determined by topography and stratification. Bottom and interior advective fluxes increase rapidly with time before approaching an asymptotic value, and can be characterized by a simple expression of the type

$$F(t) = (F_m - F_0)\left(1 - e^{-t/T}\right) + F_0, \tag{8}$$

where nitrate flux (F) at time t is described by a characteristic maximum flux (F_m), initial flux (F_0), and time scale (T). Similarly, upwelling source depth as calculated in section 4.1.2 can be approximated by

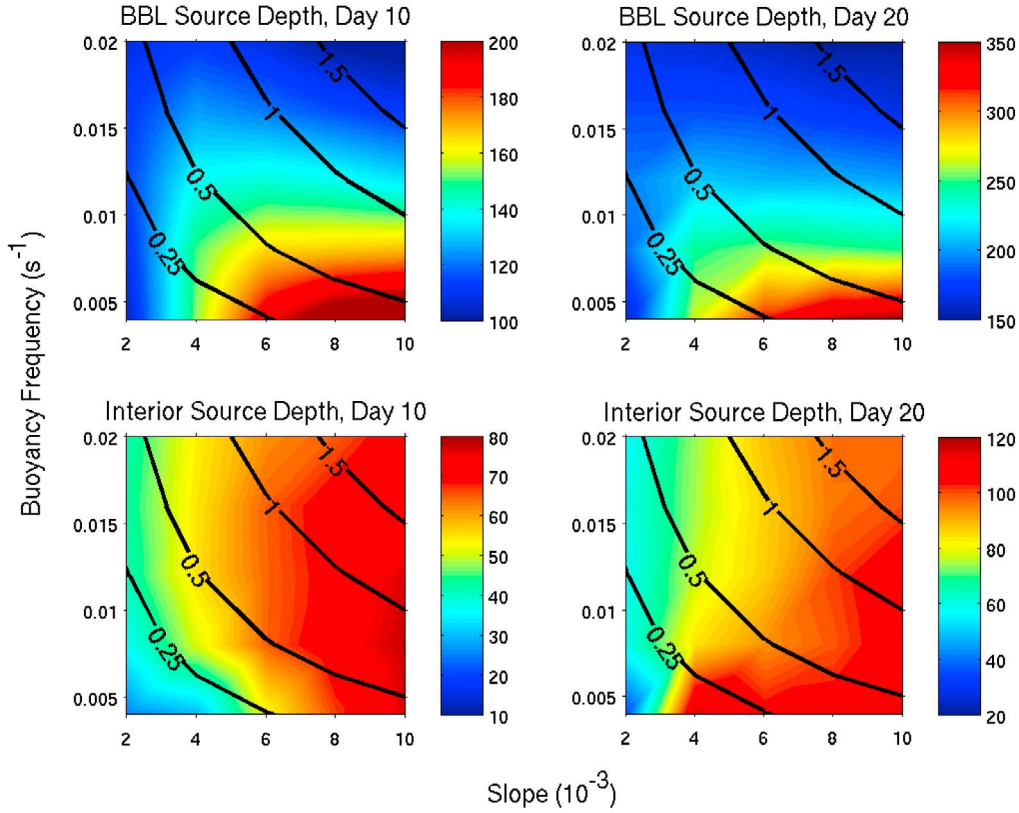$$d(t) = (d_m - d_0)\left(1 - e^{-t/T}\right) + d_0, \tag{9}$$

Figure 9. Upwelling source depths (m) for (top) BBL and (bottom) interior nitrate fluxes after 10 and 20 days, with Burger number indicated by contours. As in Figure 7, 25 model runs are represented spanning a range of slope and stratification. Note different color scales for each.

where the flux (F) terms in equation (8) are replaced by depth (d) terms in equation (9). For each model run, nitrate flux (or source depth) is fit using values of T, $F_0(d_0)$, and $F_m(d_m)$ that minimize model-data misfit in a least squares sense. These values are then parameterized by physical properties of the water column (α, N) as outlined in Table 2. As mentioned previously, the effect of Coriolis frequency on nitrate flux is complicated. All model experiments used for development of the empirical model have $f = 10^{-4}$ s^{-1}, so parameters that appear to vary with Burger number are reported as functions of αN rather than S. The F_0 and d_0 terms represent nonzero flux and source depth at $t = 0$ and are not strictly accurate for a system initiated from rest. However, immediately following the onset of upwelling favorable winds, a finite inner shelf region is established. Since we calculate BBL nitrate flux and source depth at the inner shelf boundary, the empirical model is best configured with a nonzero initial condition associated with the inner shelf extent shortly after initialization. While interior flux and source depth are independent of the inner shelf definition, an analogous effect could be produced by rapid development of the SML. We find this effect to be small and configure the interior flux and source depth equations with $F_0 = d_0 = 0$.

[28] The time scale for BBL nitrate flux evolution is not representative of the flow itself, but rather how quickly BBL transport draws from depths below the nitrate maximum at 200 m. Beyond this time no greater nitrate can be transported to the surface, even as source depth increases. Weak strati-
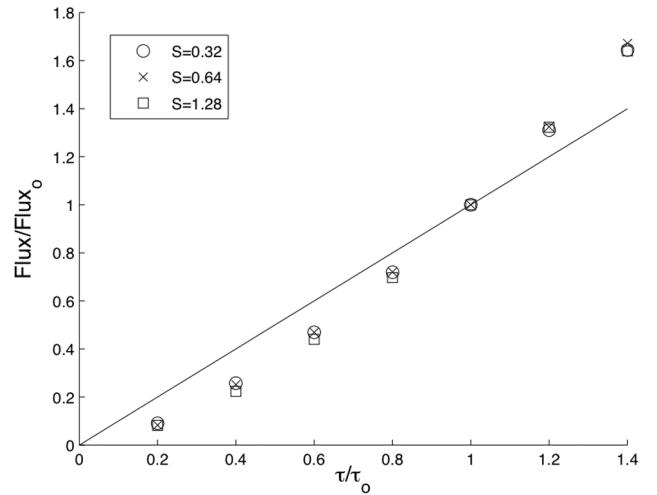

Figure 10. Scaling of BBL nitrate flux relative to wind stress. Surface wind stress and BBL flux are scaled by the base case where $\tau_o = 0.1$ N m^{-2}. A total of 21 model runs are shown; three Burger number configurations each run with seven wind stress magnitudes ranging from 20–140% of τ_o. The solid line plotted for reference is theoretical scaling of cross-shelf transport with wind stress. Flux ratios are averaged from day 10–15.
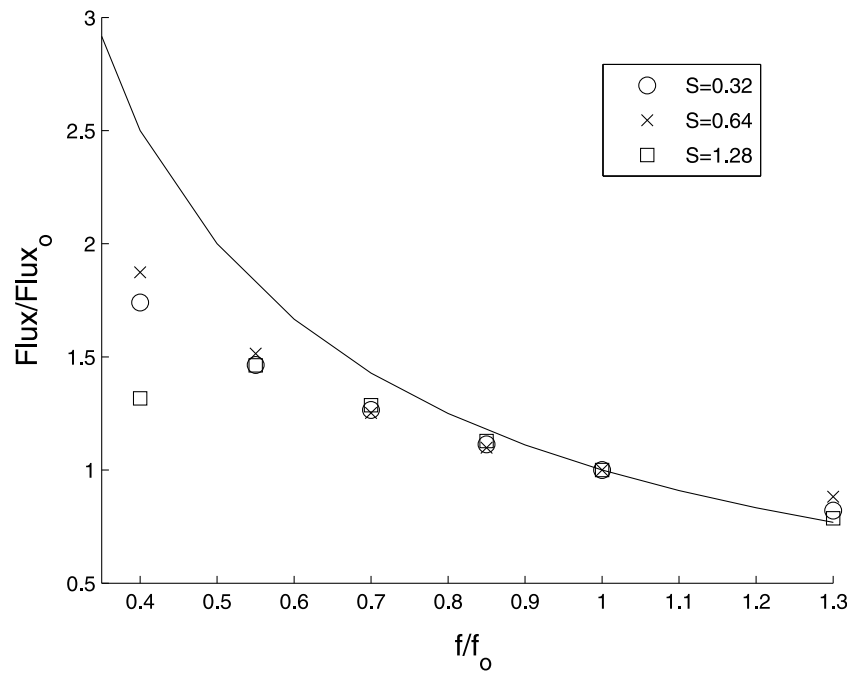
Figure 11. Scaling of BBL nitrate flux relative to Coriolis frequency. Scaling is performed as in Figure 10, with a base case of $f_o = 10^{-4}\,\text{s}^{-1}$. Solid line indicates theoretical scaling of cross-shelf transport with Coriolis frequency. Note that Burger number values in the legend only apply to the base case, as Burger number changes with f.

fication concentrates transport in the BBL and steep slope allows deep water the shortest horizontal travel to reach the inner shelf. As a result, time scales for evolution of BBL nitrate flux increase with the ratio of N to α, from $T \approx 3$ days at $N/\alpha = 0.4\,\text{s}^{-1}$ to $T \approx 12$ days at $N/\alpha = 10\,\text{s}^{-1}$. In the interior, source depths are shallower than those in the BBL, and nitrate flux is not quickly limited by the nitrate maximum at 200 m depth. For cases with significant interior nitrate flux ($S \geq 0.6$), time scales for nitrate flux evolution are fairly steady, with $T = 19.4 \pm 3.3$ days. Time scales for evolution of the BBL and interior source depth were also empirically determined and are $T = 17.6 \pm 2.6$ days and $T = 10.7 \pm 1.1$ days, respectively.

[29] Figure 5 shows fluxes produced by the numerical and analytical (equation (8)) models. Not surprisingly, maximum BBL nitrate flux is greatest with weak slope and stratification. Given sufficient time, BBL transport draws from below the nitrate maximum in all cases. Maximum BBL flux is therefore dependent on the fraction of onshore transport occurring in the BBL, shown by LC to decrease as αN increases. The analytical model overestimates BBL fluxes in the case of weakest slope and stratification (α =

0.002, $N = 0.004\,\text{s}^{-1}$) where an extremely thick BBL results in low onshore velocities even though total BBL transport is high. Consequently, deep nitrate-rich water reaches the inner shelf slowly. Agreement is good through the rest of the parameter range. As interior transport increases with αN, so does maximum interior nitrate flux. At $\alpha N = 0$, onshore flow occurs entirely in the BBL and interior nitrate flux vanishes. At $\alpha N = 2 \times 10^{-4}\,\text{s}^{-1}$ ($S = 2$ in our experiments), maximum steady state nitrate flux in the interior approaches 20 mmol s^{-1}, about two thirds the maximum BBL flux as S approaches zero.

[30] For constant wind stress and Coriolis frequency, maximum BBL source depth is set by stratification (Table 2). In contrast, maximum interior source depth is determined primarily by slope. The influence of slope is seen clearly on day 10 and day 20 (Figure 9), though stratification appears to become more important with time. If the empirical model were based on longer model runs, stratification would likely emerge in the interior source depth parameterization. Source depth estimates based on equation (9) and parameters in Table 2 are shown in Figure 8 and agree well with estimates obtained from the numerical model.

Table 2. Parameters for Analytical Nitrate Flux and Source Depth Expressions[a]

Modeled Parameter	F_0 or d_0 (mmol s^{-1} or m)	F_m or d_m (mmol s^{-1} or m)	T (days)
BBL NO$_3$ Flux	1.6 ± 0.8	$27.6e^{-\alpha N/5.1 \times 10^{-5}} + 5.7$	$11.9e^{-\alpha/0.45N} + 2.9$
Interior NO$_3$ Flux	0	$19.2(1 - e^{-\alpha N/9.4 \times 10^{-5}})$	19.4 ± 3.3
BBL Source Depth	20.5 ± 4.7	$495e^{-N/0.0080} + 182$	17.6 ± 2.6
Interior Source Depth	0	$104e^{-0.0058/\alpha} + 65$	10.7 ± 1.1

[a]F_o relates to flux parameters and d_o relates to source depth parameters. Similarly, F_m and d_m relate to flux parameters and source depth parameters, respectively. All expressions assume $f = 10^{-4}\,\text{s}^{-1}$.
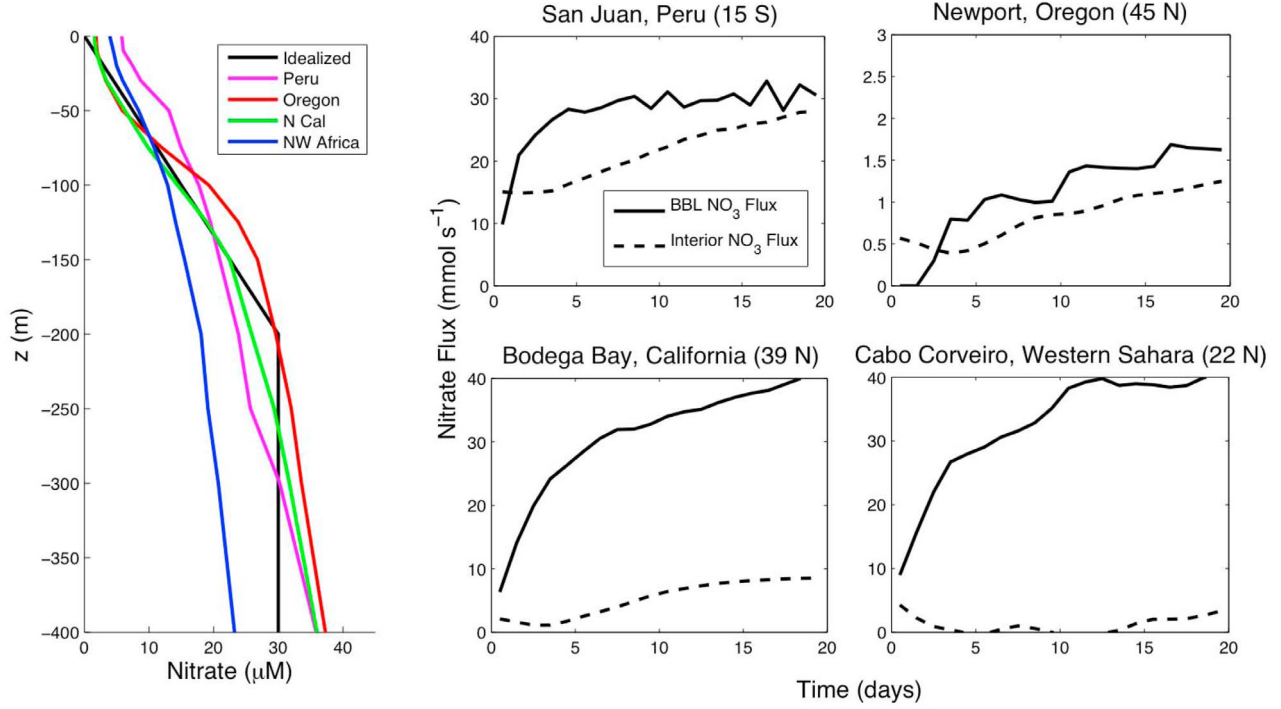
Figure 12. Idealized 2-D numerical model applied to global upwelling regions. (left) Annual average nitrate profiles for each region, gathered from the World Ocean Atlas 2005 database. Other parameters for each case (latitude, stratification, slope, wind stress) are outlined in Table 1. (right) Interior and BBL fluxes calculated from model output for each region. Note the scale for Oregon is different from the other cases.

[31] While equation (8) is able to accurately describe modeled nitrate fluxes, it is based on an idealized initial nitrate profile. To generalize the application of the empirical model to varied nitrate profiles, we represent nitrate flux as the product of theoretical steady state transport in the BBL or interior (U_{BBL} or U_{INT}) and initial nitrate concentration at a characteristic source depth ($[NO_3]_S$), obtained from the numerical model

$$F = U[NO_3]_S \qquad (10)$$

$$U_{BBL} = \frac{\tau}{\rho_0 f} \frac{1 - S/2}{1 + S/2} \qquad U_{INT} = \frac{\tau}{\rho_0 f} \frac{S}{1 + S/2}. \qquad (11)$$

LC derived equation (11), where τ is alongshore surface wind stress and ρ_0 is a reference density. This form has the advantage of being applied to any initial nitrate profile, based on the source depth evolution (equation (9)). Application of equations (10) and (11) to our test cases is shown in Figure 6 along with calculated nitrate fluxes. In these model runs, the idealized linear nitrate profile was replaced with a real profile taken off the Oregon coast. Agreement is good for interior flux estimates at all but the highest Burger numbers, and for BBL estimates on $0.16 \leq S \leq 1.2$. At high Burger numbers, divergence of modeled BBL transport from LC theory (Figure 2) causes the empirical model to underestimate BBL nitrate flux and overestimate the interior contribution.

4.3. Global Upwelling Regions

[32] Between the four EBC locations studied by LC, Coriolis and buoyancy frequencies vary almost threefold, shelf slopes change by a factor of six, and there is nearly an order of magnitude range in Burger number. It is reasonable that these parameters should strongly influence the productivity of upwelling regions and the differences between them. In order to investigate the simplified model in real upwelling systems, model runs were performed for the four locations described in LC. Stratification and topographic slope are still constant, but have magnitudes representative of each location. Surface forcing is also idealized, with no spatial or temporal variability, but its magnitude is determined from QuikSCAT data. For each location, we use daily wind stress for 2007–2008, and take the mean alongshore component from a three month upwelling season. Realistic nitrate profiles for each region are obtained from the World Ocean Atlas 2005 Database annual averages [*Garcia et al.*, 2006]. Figure 12 and Table 1 outline the input parameters for all cases. Results from the idealized model with the given configurations are shown in Figure 12. It is important to note that each case is a discrete location within an upwelling system, and is not representative of the system as a whole.

[33] Substantial differences in BBL and interior nitrate flux contributions between several upwelling sites are apparent. The two high Burger number locations, off Peru and Oregon, show significant contributions from the interior. BBL and interior fluxes off Peru are comparable over the first 20 days,
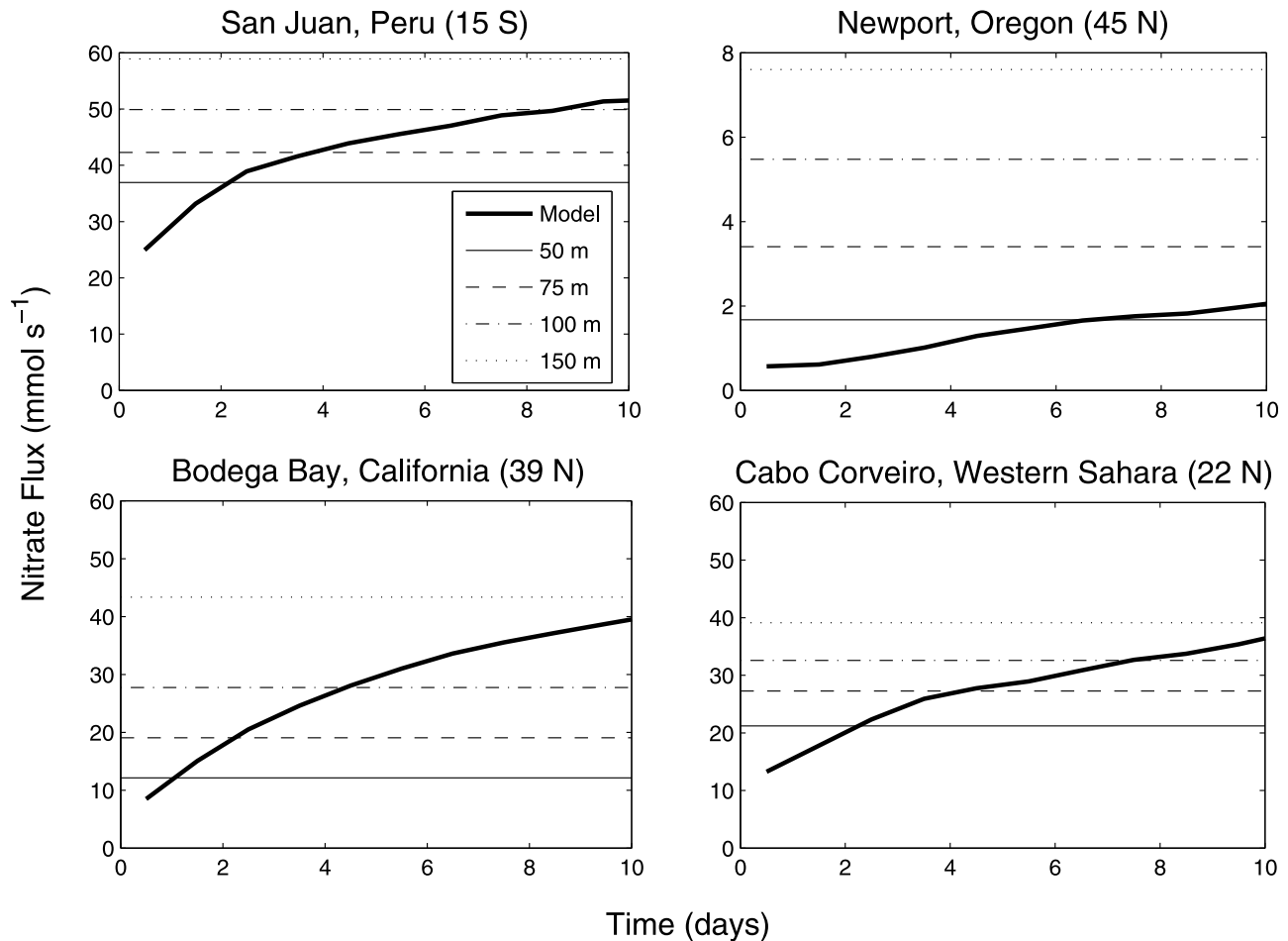
Figure 13. Total (interior and BBL) advective nitrate flux for locations in major global upwelling regions. Thick lines represent numerical model output. Additional estimates (thin lines) are calculated as the product of theoretical Ekman transport and nitrate concentration at various source depths. Ekman transport is estimated based on parameters in Table 1. Nitrate concentrations at 50, 75, 100, and 150 m depths come from the World Ocean Atlas 2005 database. Note the scale for Oregon is different from the other cases.

with steady BBL flux after a brief initial spin-up and interior flux that rises slightly with time. Nitrate concentration off Peru is relatively high in the upper 50 m, allowing rapid transport to the SML by strong interior flow. Interior and BBL nitrate fluxes are also comparable to each other at the Oregon site; however both are very low in magnitude due to the weak surface forcing used in the model. It should be noted that on an event scale, surface wind stress off Oregon can often reach 0.1–0.2 N m^{-2}, much higher than the mean value of 0.03 N m^{-2} used here. Nitrate fluxes associated with the higher event-scale wind stress could reach values on par with the other three locations shown in Figure 12. In contrast with the Peru and Oregon sites examined, the northern California and northwest Africa sites are dominated by BBL nitrate flux, with a negligible interior contribution in the latter case. Also, while Ekman transport off northern California is significantly less than that off northwest Africa (based on wind stress and latitude in Table 1), their BBL nitrate fluxes are approximately equal owing to the much richer deep nitrate stock of the Pacific relative to the Atlantic. At model day 10, total nitrate advection is highest at the Peru site (~50 mmol s^{-1}),

slightly lower at the northern California and northwest Africa locations (~40 mmol s^{-1}), and much lower off Newport, Oregon (~2 mmol s^{-1}). Though transport in the Canary Current case is strong and entirely in the BBL, total flux is limited by low nitrate concentrations in the deep north Atlantic and a very weakly sloping shelf that makes deep water available only far offshore.

[34] Figure 13 illustrates nitrate flux dependence on upwelling source depth. During much of the first 10 days of upwelling, nitrate fluxes at our Peru and northwest Africa sites are bracketed by estimates using source depths of 50 m and 100 m. In comparison, source depth off northern California increases rapidly due to strong surface forcing, while the opposite is true in the weakly forced Newport, Oregon case. As reported elsewhere [*Messié et al.*, 2009], nitrate flux estimates in the California Current are much more sensitive to choice of source depth than either the Peru or Canary Currents. The increase in nitrate flux estimated using 100 m source depth compared to 50 m, for example, is highly dependent on region. In our test cases off Peru and northwest Africa, differences are 13.0 mmol s^{-1} (35%) and

11.4 mmol s^{-1} (54%), respectively. In the California Current, differences are 15.6 mmol s^{-1} (129%) for northern California and 3.8 mmol s^{-1} (228%) for Oregon.

5. Discussion

[35] *Lentz and Chapman* [2004] demonstrated that the structure of cross-shelf flow during upwelling is dependent on a topographic Burger number. As Burger number increases, bottom stress decreases and onshore transport shifts from the BBL to the interior of the water column. These findings motivated our investigation into the resulting impacts on nutrient supply in upwelling regions. For example, how do nutrient fluxes in strongly stratified, high-latitude waters off Oregon differ from those in weakly stratified, low-latitude waters over the steep continental shelf of Peru?

[36] The suite of numerical model simulations described here shows the dependence of interior, BBL, and total nitrate flux on topographic slope, stratification, wind stress, and latitude. The distinction of interior and BBL transport allows quantification of nitrate fluxes to discrete cross-shelf regions in the upwelling zone. Specifically, BBL transport supplies the inner shelf while interior transport supplies the mid- and outer shelf. For an idealized initial nitrate profile, interior and BBL advective nitrate fluxes vary with Burger number. Low Burger numbers produce a greater fraction of transport, and consequently nitrate flux, in the BBL while higher Burger numbers increase the interior contribution. Consequently, the inner shelf, often characterized by high productivity and retention inshore of the upwelling front, may be favored for production in low Burger number regions with a large fraction of onshore transport in the BBL. In contrast, strong stratification and a steeply sloping shelf may produce a relatively small inner shelf region with less nutrient input to fuel potential production. Vertical diffusion is a relatively small contributor to nitrate flux, but is greater in weakly stratified systems. Increased surface nitrate due to mixed layer deepening is greatest in weakly stratified cases, which produce the deepest mixed layers. It is also greater in steep slope cases where high nitrate is carried to the base of the SML by strong interior flow and subsequently entrained. These results are not specific to any particular region, but provide insight into how nitrate supply is affected by physical parameters that govern many upwelling systems.

[37] Observations, theory, and numerical model results show distinct bottom and interior cross-shelf flow regimes [*Smith*, 1981; *Lentz and Chapman*, 2004] and during sustained upwelling, source depths for each of these regimes increase with time (Figure 8). However, observational studies of upwelling fluxes are generally limited to choosing a single characteristic source depth for a given region [e.g., *Chavez and Barber*, 1987; *Walsh*, 1991; *Messié et al.*, 2009]. The sensitivity of nitrate flux to upwelling source depth is dependent on the local nitrate profile in the region of interest. On an event time scale of days, we find that source depth estimates of 50–100 m appear reasonable for all locations, though the northern California site reaches these depths quickly while the weak forcing used off Oregon produces relatively shallow source water (Figure 13). A thorough analysis of appropriate source depth for a given upwelling region should therefore consider not only physical characteristics of the region but also temporal variability of sur-

face winds. Spectral analysis of the wind field at a given location would inform the choice of source depth by indicating a typical upwelling duration. Based on the intersection of offshore and inshore T-S diagrams, *Messié et al.* [2009] note typical upwelling source depths of 75, 60, and 100 m for the Peru, California, and Canary systems, respectively.

[38] The model runs described in section 4.3 examine upwelling fluxes at several discrete locations in major upwelling systems. Though separated by less than 1000 km, our two California Current sites (near Bodega Bay, California and Newport, Oregon) differ drastically in terms of modeled nitrate flux. The largest difference between the two is the magnitude of nitrate flux, which can be attributed to surface forcing. The mean upwelling favorable wind stress used to force our model is 0.18 N m^{-2} off northern California, compared to just 0.03 N m^{-2} off central Oregon. On an event scale, however, wind stress at Newport, Oregon can reach 0.1–0.2 N m^{-2}, producing nitrate fluxes similar to those modeled at our northern California site. In either case, the two locations differ significantly in the structure of onshore flow. Strong stratification off Newport, Oregon produces a Burger number more than double that at the northern California site. Consequently, there is substantial onshore transport in the interior off Oregon, and very little off northern California. It should be noted that while our chosen California Current sites show a steeper shelf off Oregon than northern California, this is actually counter to the general latitudinal trend in shelf width from California to Washington [*Hickey and Banas*, 2008]. Thus, selection of different sites could result in a higher Burger number off northern California, a lower Burger number off Oregon, and much more similar structures in cross-shelf transport. At both locations, and especially Newport, upwelling favorable winds persist over much less of the year than at the Peru and northwest Africa sites. The event-scale nitrate fluxes depicted in Figure 12 are therefore likely to be limited to the relatively short and intense spring/summer upwelling season. Also, the persistence of upwelling favorable alongshore winds is rarely longer than 10 days between relaxations or reversals [*Kudela et al.*, 2006], so upwelling source depth may be unlikely to reach the depths indicated by our model beyond 10 days.

[39] It is well known from previous modeling [*McCreary*, 1981; *Federiuk and Allen*, 1995] and observational [*Allen and Smith*, 1981; *Lentz*, 1994] studies that an alongshore pressure gradient, resulting from a poleward decrease in sea surface height, can modify dynamics of eastern boundary upwelling systems. LC have shown that for a given Burger number, bottom stress is reduced by an alongshore pressure gradient consistent with a poleward decrease in sea surface height, and for a given alongshore pressure gradient, the relative change to the bottom stress is larger for smaller Burger numbers. Our model does not include this effect but we consider here its qualitative impact. A reduction in bottom stress reduces BBL transport, effectively shifting the partitioning of onshore transport from the BBL to the interior. As a result, we expect the addition of an alongshore pressure gradient to be qualitatively similar, with respect to nutrient fluxes, to an increase in Burger number. The magnitude of this effect and its quantitative significance are left to a further study.

[40] The Canary Current site discussed in LC and used here to initialize the 'NW Africa' model has the lowest Burger

number ($S = 0.19$) of the four locations, due largely to its very weakly sloping shelf. At such low Burger number, approximately 90% of modeled transport occurs in the BBL (Figure 2), promoting efficient upwelling of macronutrients and in nature, potentially iron. *Messié et al.* [2009] show a strong latitudinal gradient at ~21°N for both nitrate at 60 m and estimated nitrate supply in the Canary Current. To the south, nitrate at 60 m reaches 20 μmol L^{-1} and nitrate flux due to coastal upwelling is 20–25 mmol s^{-1}. To the north, nitrate at 60 m drops to near zero and nitrate flux is ~5 mmol s^{-1}. Our Canary Current model is configured at 22°N, near the border of the north and south regions. While modeled fluxes (Figure 13) indicate this location is more representative of the south than the north, it likely underestimates nitrate fluxes south of 20°N. *Barton et al.* [1977] describe the offshore movement of the upwelling core in the Canary Current near Cabo Corveiro, where the coldest waters are initially near shore (as in our model), but migrate offshore with sustained upwelling favorable winds. The upwelling core ultimately remains at the shelf break (~100 m water depth) and inshore of this is a retentive and highly productive region [*Estrade et al.*, 2008]. Our linearized topography is unable to represent the impact of the shelf break; however the model does show a rapid offshore movement of the upwelling front given the slope and stratification at our northwest Africa location (Figure 4).

[41] Due to its low latitude and steep shelf, the Peru site has the highest Burger number of the four investigated here. Consequently, the interior contribution to nitrate flux is greater in this case than any other. At the Burger number of this site ($S = 1.35$), approximately 80% of volume transport is concentrated in the interior of the water column (Figure 2), and about half of all nitrate flux derives from the interior (Figure 12). The nitrate profile at our Peru location differs from the other regions in that high nitrate is available close to the surface. Following the onset of upwelling favorable winds, this nitrate is readily available and rapidly enters the SML from both the interior and BBL. In the first day of upwelling, advective nitrate flux off Peru is double that of any of the other locations. In brief periods of upwelling winds, this region may be able to fuel more production than others. However, the large fraction of interior transport may lead to conditions with insufficient iron available for efficient uptake of nitrate. As upwelling winds persist, source depth increases, but nitrate flux is affected little due to a relatively weak vertical nitrate gradient. Consequently, nitrate fluxes based on a constant source depth model are not particularly sensitive to selection of upwelling source depth.

[42] Not accounted for in our model are the shelf break and continental slope, both important components of boundary topography. It is interesting to speculate on how their inclusion may influence our results. The bottom slope is much greater over the continental slope than it is on the continental shelf; deep water offshore of the shelf break is therefore horizontally closer to shore than in our model. Upwelling circulation that draws from beyond the shelf break should reduce the time scale for deep water reaching the SML and increase overall nitrate flux. However, this effect may be complicated by changed upwelling dynamics near the shelf break, such as those outlined in the northwest Africa case. We leave quantitative evaluation of these effects to further study.

[43] While comparisons of modeled nitrate fluxes in the present analysis to ecosystem-scale studies of potential and observed productivity [*Carr*, 2002; *Carr and Kearns*, 2003; *Messié et al.*, 2009] are tempting, there are several important caveats in doing so: (1) our model experiments each represent an idealized 2-D approximation to a coastline with variable bathymetry and 3-D circulation (our topography omits important features such as the shelf break, continental slope, capes, and canyons); (2) each model run represents a single location within an upwelling ecosystem and not some average of the entire ecosystem; (3) this approach focuses on nitrate upwelling dynamics on an event scale, not a seasonal, annual, or interannual scale; (4) we do not consider upwelling driven by wind stress curl, whose contribution is uncertain, with estimates ranging from small [*Messié et al.*, 2009] to equal or greater than coastal upwelling [*Pickett and Paduan*, 2003; *Dever et al.*, 2006; *Rykaczewski and Checkley*, 2008]; and (5) only new production is supported by upwelled nitrate, not total primary production. The ratio of new to total primary production (the f ratio) may vary among upwelling regions based on factors such as light availability, mixed layer depth, limitation by other nutrients [*Messié et al.*, 2009], and wind speed [*Botsford et al.*, 2003]. Results presented here cannot characterize entire upwelling ecosystems in a spatially and temporally averaged sense, but do illustrate some differences between them.

[44] The analytical expressions presented in section 4.2 come from the combination of a previously developed steady state transport theory (LC) and diagnostics from our numerical model. Nitrate flux and source depth predicted by the diagnostic model are presented for ranges of shelf slope and stratification that cover those encountered in major global upwelling regions. Though empirical, the analytical model works well throughout most of the range of Burger numbers tested and has several benefits. First, it provides estimates of time-dependent nitrate (or other macronutrient) flux in upwelling regions as a function of topographic slope, stratification, and initial nutrient profile. Second, the asymptotic form of the analytic expressions allows for steady state estimates of flux and source depth. Third, it provides a basis for qualitative comparison of potential new production among upwelling regions based on their physical properties. Fourth, expressions for source depth can be applied to questions beyond nitrate flux, such as micronutrient supply. It is important to note that fluxes into the SML after 2 days of sustained upwelling are not equal to those after 10 days. Here, this temporal development is represented.

[45] In addition to comparisons between upwelling regions, one can apply the present approach to change in one region over time. Based on long-term temperature records in the CCS, *Palacios et al.* [2004] found increased thermal stratification near the coast from 1950–1993, presumably inhibiting upwelling of nutrients. However, increased upwelling-favorable winds due to greenhouse gas forcing have been hypothesized [*Bakun*, 1990] and supported in the CCS by observations [*Schwing and Mendelssohn*, 1997]. *Di Lorenzo et al.* [2005] concluded that any upwelling increase due to strengthened upwelling favorable winds over the last 50 years has been negated by increased stratification and thermocline deepening in the CCS. *Auad et al.* [2006] found the opposite in future projections, with an overall increase in upwelling due to dominance of increased upwelling favorable

winds. *García-Reyes and Largier* [2010] noted increased upwelling along the central California coast from 1982–2008. While it is beyond the scope of this paper, the idealized model could be configured with either past or projected winds, stratification, and nitrate profiles to provide an alternate prediction.

[46] Further, our idealized model approach may be applied to a number of questions not addressed here. The first, which has been discussed briefly, is the impact of shelf slope and stratification on micronutrient supply. *Johnson et al.* [1999] found that the primary source of iron in the CCS is resuspension and subsequent upwelling of particles in the BBL. As such, we expect upwelling sites with substantial onshore flow along the sediments to be iron replete. In areas of high Burger number and interior flow, iron limitation may curb productivity. One example is the contrast of the wide shelf and iron-replete conditions from Monterey Bay to Pt. Reyes with the narrow shelf and iron-deplete conditions off the Big Sur coast south of Monterey Bay [*Bruland et al.*, 2001]. A second question relates to hypoxia at upwelling sites. Hypoxic conditions have been frequently observed in the CCS over both the Oregon and Washington continental shelves [*Chan et al.*, 2008; *Connolly et al.*, 2010] and could be related to upwelling circulation. For example, strong stratification may produce onshore transport concentrated in the interior, thus limiting ventilation of bottom waters over the continental shelf and promoting hypoxia near the bottom. Alternatively, strong and prolonged BBL transport may entrain low-oxygen waters from the continental slope onto the shelf. Finally, the structure of cross-shelf flow has implications for redistribution of phytoplankton communities from the sediments and within the water column. During unfavorable growth conditions, mass sinking can be a survival mechanism for diatoms that remain viable longer in cold, dark water than warm, nutrient depleted water [*Smetacek*, 1985]. Dinoflagellates also react to unfavorable conditions by sinking, through the formation of nonmotile cysts. In high Burger number regions, sinking cells may find adequate nutrients and light just below the SML, as well as onshore flow that keeps cells entrained near the coast [*Batchelder et al.*, 2002]. Cells that sink to the sea floor may ultimately be carried onshore by BBL flow more efficiently in low Burger number regions. In either case, the structure of onshore flow could play an important role in transporting a small seed population to the SML when favorable growth conditions return.

References

Allen, J. S., and R. L. Smith (1981), On the dynamics of wind-driven shelf currents, *Philos. Trans. R. Soc. A*, *302*, 617–634.

Allen, J. S., P. A. Newberger, and J. Federiuk (1995), Upwelling circulation on the Oregon continental shelf. Part I: Response to idealized forcing, *J. Phys. Oceanogr.*, *25*, 1843–1866.

Auad, G., A. Miller, and E. Di Lorenzo (2006), Long-term forecast of oceanic conditions off California and their biological implications, *J. Geophys. Res.*, *111*, C09008, doi:10.1029/2005JC003219.

Austin, J. A., and S. J. Lentz (2002), The inner shelf response to wind-driven upwelling and downwelling, *J. Phys. Oceanogr.*, *32*, 2171–2193.

Bakun, A. (1990), Global climate change and intensification of coastal ocean upwelling, *Science*, *247*, 198–201.

Barton, E. D., A. Huyer, and R. L. Smith (1977), Temporal variation observed in the hydrographic regime near Cabo Corveiro in the northwest African upwelling region, February to April 1974, *Deep Sea Res.*, *24*, 7–23.

Batchelder, H. P., C. A. Edwards, and T. M. Powell (2002), Individual-based models of copepod populations in coastal upwelling regions: Implications of physiologically and environmentally influenced diel vertical migration on demographic success and nearshore retention, *Prog. Oceanogr.*, *53*, 307–333.

Botsford, L. W., C. A. Lawrence, E. P. Dever, A. Hastings, and J. L. Largier (2003), Wind strength and biological productivity in upwelling systems: An idealized study, *Fish. Oceanogr.*, *12*, 245–259.

Bruland, K. W., E. L. Rue, and G. J. Smith (2001), Iron and macronutrients in California coastal upwelling regimes: Implications for diatom blooms, *Limnol. Oceanogr.*, *46*, 1661–1674.

Carr, M. E. (2002), Estimation of potential productivity in eastern boundary currents using remote sensing, *Deep Sea Res. Part II*, *49*, 59–80.

Carr, M. E., and E. J. Kearns (2003), Production regimes in four eastern boundary current systems, *Deep Sea Res. Part II*, *50*, 3199–3221.

Chan, F., J. A. Barth, J. Lubchenco, A. Kirincich, H. Weeks, W. T. Peterson, and B. A. Menge (2008), Emergence of anoxia in the California Current large marine ecosystem, *Science*, *319*, 920.

Chapman, D. C., and S. J. Lentz (2005), Acceleration of a stratified current over a sloping bottom, driven by an alongshelf pressure gradient, *J. Phys. Oceanogr.*, *35*, 1305–1317.

Chavez, F. P., and R. T. Barber (1987), An estimate of new production in the equatorial Pacific, *Deep Sea Res. Part A*, *34*, 1229–1243.

Chavez, F. P., and M. Messié (2009), A comparison of eastern boundary upwelling ecosystems, *Prog. Oceanogr.*, *83*, 80–96, doi:10.1016/j.pocean.2009.07.032.

Chavez, F. P., and J. R. Toggweiler (1995), Physical estimates of global new production: The upwelling contribution, in *Upwelling in the Ocean: Modern Processes and Ancient Records*, edited by C. P. Summerhayes et al., pp. 313–320, John Wiley, New York.

Connolly, T. P., B. M. Hickey, S. L. Geier, and W. P. Cochlan (2010), Processes influencing seasonal hypoxia in the northern California Current System, *J. Geophys. Res.*, *115*, C03021, doi:10.1029/2009JC005283.

Dever, E. P., C. E. Dorman, and J. L. Largier (2006), Surface boundary layer variability off northern California, USA during upwelling, *Deep Sea Res. Part II*, *53*, 2887–2905.

Di Lorenzo, E., A. J. Miller, N. Schneider, and J. C. McWilliams (2005), The warming of the California Current System: Dynamics and ecosystem implications, *J. Phys. Oceanogr.*, *35*, 336–362.

Dugdale, R. C., and J. J. Goering (1967), Uptake of new and regenerated forms of nitrogen in primary productivity, *Limnol. Oceanogr.*, *12*, 196–206.

Estrade, P., P. Marchesiello, A. Colin de Verdiere, and C. Roy (2008), Cross-shelf structure of coastal upwelling: A two-dimensional expansion of Ekman's theory and a mechanism for innershelf upwelling shut down, *J. Mar. Res.*, *66*, 589–616.

Federiuk, J., and J. S. Allen (1995), Upwelling circulation on the Oregon continental shelf. Part II: Simulations and comparisons with observations, *J. Phys. Oceanogr.*, *25*, 1867–1889.

Garcia, H. E., R. A. Locarnini, T. P. Boyer, and J. I. Antonov (2006), *World Ocean Atlas 2005*, vol. 4, *Nutrients (Phosphate, Nitrate, and Silicate), NOAA Atlas NESDIS*, vol. 64, edited by S. Levitus, 396 pp., NOAA, Silver Spring.

García-Reyes, M., and J. Largier (2010), Observations of increased wind-driven coastal upwelling off central California, *J. Geophys. Res.*, *115*, C04011, doi:10.1029/2009JC005576.

Haidvogel, D. B., et al. (2008), Ocean forecasting in terrain-following coordinates: Formulation and skill assessment of the Regional Ocean Modeling System, *J. Comput. Phys.*, *227*, 3595–3624.

Hickey, B. M., and N. S. Banas (2008), Why is the northern end of the California Current System so productive?, *Oceanography*, *21*(4), 90–107.

Johnson, K. S., F. P. Chavez, and G. E. Friederich (1999), Continental-shelf sediment as a primary source of iron for coastal phytoplankton, *Nature*, *398*, 697–700.

Kudela, R. M., N. Garfield, and K. W. Bruland (2006), Bio-optical signatures and biogeochemistry from intense upwelling and relaxation in coastal California, *Deep Sea Res. Part II*, *53*, 2999–3022.

Laanemets, J., V. Zhurbas, J. Elken, and E. Vahtera (2009), Dependence of upwelling-mediated nutrient transport on wind forcing, bottom topography and stratification in the Gulf of Finland: Model experiments, *Boreal Environ. Res.*, *14*, 213–225.

Large, W. G., J. C. McWilliams, and S. C. Doney (1994), Oceanic vertical mixing: A review and a model with a vertical K-profile boundary layer parameterization, *Rev. Geophys.*, *32*, 363–403.

Lentz, S. J. (1992), The surface boundary layer in coastal upwelling regions, *J. Phys. Oceanogr.*, *22*, 1517–1539.

Lentz, S. J. (1994), Current dynamics over the northern California inner shelf, *J. Phys. Oceanogr.*, *24*, 2461–2478.

Lentz, S. J., and D. C. Chapman (2004), The importance of non-linear cross-shelf momentum flux during wind-driven coastal upwelling, *J. Phys. Oceanogr.*, *34*, 2444–2457.

McCreary, J. P. (1981), A linear stratified ocean model of the coastal undercurrent, *Philos. Trans. R. Soc. A*, *302*, 385–413.

Messié, M., J. Ledesma, D. D. Kolber, R. P. Michisaki, D. G. Foley, and F. P. Chavez (2009), Potential new production estimates in four eastern boundary upwelling ecosystems, *Prog. Oceanogr.*, *83*, 151–158, doi:10.1016/j.pocean.2009.07.018.

Palacios, D. M., S. J. Bograd, R. Mendelssohn, and F. B. Schwing (2004), Long-term and seasonal trends in stratification in the California Current, 1950–1993, *J. Geophys. Res.*, *109*, C10016, doi:10.1029/2004JC002380.

Pauly, D., and V. Christensen (1995), Primary production required to sustain global fisheries, *Nature*, *374*, 255–257.

Pickett, M. H., and J. D. Paduan (2003), Ekman transport and pumping in the California Current based on the U.S. Navy's high-resolution atmospheric model (COAMPS), *J. Geophys. Res.*, *108*(C10), 3327, doi:10.1029/2003JC001902.

Pollard, R., P. B. Rhines, and R. O. R. Y. Thompson (1973), The deepening of the wind-mixed layer, *Geophys. Fluid Dyn.*, *3*, 381–404.

Rykaczewski, R. R., and D. M. Checkley (2008), Influence of ocean winds on the pelagic ecosystem in upwelling regions, *Proc. Natl. Acad. Sci.*, *105*, 1965–1970.

Schwing, F. B., and R. Mendelssohn (1997), Increased coastal upwelling in the California current system, *J. Geophys. Res.*, *102*, 3421–3438.

Shchepetkin, A. F., and J. C. McWilliams (2005), The Regional Ocean Modeling System: A split-explicit, free-surface, topography following coordinates ocean model, *Ocean Modell.*, *9*, 347–404.

Smetacek, V. S. (1985), Role of sinking in diatom life-history cycles: Ecological, evolutionary and geological significance, *Mar. Biol.*, *84*, 239–251.

Smith, R. L. (1981), A comparison of the structure and variability of the flow field in three coastal upwelling regions: Oregon, Northwest Africa, and Peru, in *Coastal Upwelling*, pp. 107–118, edited by F. A. Richards, AGU, Washington, D. C.

Umlauf, L., and H. Burchard (2003), A generic length-scale equation for geophysical turbulence models, *J. Mar. Res.*, *61*, 235–265.

Walsh, J. J. (1991), Importance of continental margins in the marine biogeochemical cycling of carbon and nitrogen, *Nature*, *350*, 53–55.

C. A. Edwards and M. G. Jacox, Department of Ocean Science, University of California, Santa Cruz, 1156 High St., Santa Cruz, CA 95062, USA. (mjacox@ucsc.edu)